

The Influence of Entrainment and Mixing on the Initial Formation of Rain in a Warm Cumulus Cloud

WILLIAM A. COOPER

National Center for Atmospheric Research, Boulder, Colorado

SONIA G. LASHER-TRAPP

Department of Earth, Atmospheric and Planetary Sciences, Purdue University, West Lafayette, Indiana

ALAN M. BLYTH

National Centre for Atmospheric Science, School of Earth and Environment, University of Leeds, Leeds, United Kingdom

(Manuscript received 27 April 2012, in final form 5 January 2013)

ABSTRACT

The objective of this study is to address the problem of the production of rain in warm cumulus clouds that has been observed to occur within about 20 min. A hybrid model approach is used where a microphysical parcel model is run along trajectories produced by a 3D cloud model, with sufficiently high resolution to allow explicit representation of the effects of entrainment and mixing. The model calculations take the next step from the previous study, which showed that entrainment and mixing can accelerate the diffusional growth of cloud droplets to the production of raindrops by collision and coalescence. The mechanism depends on the variability in droplet trajectories arriving at a given location and time in a cumulus cloud. The resulting broadening favors collisions among droplets in the main peak of the droplet size distribution, which leads to the production of raindrop embryos. However, this production and the subsequent growth of the embryos to become raindrops only occur in regions of relatively high cloud water content. The modeling framework allows an objective test of this sequence of events that explain the seemingly contradictory notions of the enhancement of cloud droplet growth as a result of entrainment and mixing and the need for substantial cloud water content for collision and coalescence growth. The results show that raindrops can be produced within 20 min in warm cumulus clouds. The rain produced is sensitive to giant aerosols, but modification of the modeling framework is required to conduct a more robust test of their relative importance.

1. Introduction

Significant rain forms in warm cumulus turrets in less than 20 min, as documented by Laird et al. (2000), Blyth et al. (2003), Göke et al. (2007), and others. For example, Göke et al. (2007) used radar observations of single cells from the Small Cumulus Microphysics Study (SCMS) to show that the maritime clouds of that experiment increased in radar reflectivity from -5 to $+7.5$ dBZ in a characteristic time of 333 s. Calculations of the collision-coalescence process, such as those discussed in the review by Beard and Ochs (1993) and many

others, required longer times unless the early growth occurred on sufficient numbers of “giant nuclei”—particles larger than $2\text{ }\mu\text{m}$ in diameter (e.g., Ochs 1978; Johnson 1982; Lasher-Trapp et al. 2001). Increasingly, models are able to include the significant processes that have been investigated individually over the years. For example, the 2D model of Grabowski et al. (2010) was able to produce rain at the ground in a time of 24 min. vanZanten et al. (2011) presented results of an intercomparison between 12 large-eddy simulations and also with observations made in the Rain in Cumulus over the Ocean (RICO) experiment. They found that the ensemble average of the simulations reproduced the profiles of rainwater, and to a lesser extent, the concentration of rain drops. However, there were significant differences between the models of surface precipitation rates—for example,

Corresponding author address: Alan M. Blyth, NCAS, University of Leeds, Woodhouse Lane, Leeds LS2 9JT, United Kingdom.
E-mail: a.m.blyth@leeds.ac.uk

particularly for the models with more simplified microphysics schemes.

Studies addressing the discrepancy in time have emphasized two additional candidates: (i) enhanced growth of a few of the largest cloud droplets caused by variability that results from either entrainment and mixing (e.g., Baker et al. 1980; Telford and Chai 1980; Cooper 1989) or random droplet locations (Srivastava 1989) and (ii) increase in coalescence rates that arise from turbulent enhancement of the collision rates or efficiencies (e.g., Saffman and Turner 1956; Shaw 1998; Pinsky et al. 1999a,b; Wang et al. 2008). There are many other candidate mechanisms, such as electrical effects that can change the collision efficiencies or broadening arising from aerosol components that affect condensation growth rates (e.g., Feingold and Chuang 2002). Despite these proposed explanations, the underlying discrepancy in time between observations and models has been a persistent concern for decades.

The objective of the model calculations reported in this paper is to determine if the broadening of droplet size distributions, as calculated in Lasher-Trapp et al. (2005, hereafter LCB05), can lead to an enhancement in the collision and coalescence process and the production of warm rain in convective clouds, such as those studied in SCMS. This was the original goal of Baker et al. (1980) and other studies, but it has never been possible to test because of difficulties in designing a realistic 3D model that considers the required detailed microphysics and dynamics. There is clearly a balance that hinges around the liquid water content in the cloud. Entrainment reduces the liquid water content, which is detrimental to precipitation formation (e.g., Jonas and Mason 1982, 1983). Entrainment can also broaden the droplet size distribution and produce large droplets, aiding the development of precipitation (Baker et al. 1980). In the terminology of Cooper (1989), entrainment causes droplets to experience different integral supersaturations over time while moving along nearby trajectories. However, crucially, large drops produced in this manner will only influence the subsequent development of precipitation if they then become immersed in a region of cloud with high liquid water content. Twomey (1966) performed one of the earliest modeling studies of the warm rain process. The calculations showed that the times for rain were slightly longer than the 15 min or so observed in warm oceanic clouds. Twomey suggested that the times would be reduced if regions of high liquid water content persisted in the cloud even for a short period, such as a minute.

Past studies have suggested the possibility that warm rain formation could be accelerated by the broadening of the droplet spectrum resulting from entrainment and mixing, but none could directly address the feasibility of this mechanism—that is, can the large drops resulting

from entrainment and mixing be reintroduced into regions of high liquid water content within a realistic, time-evolving 3D cumulus cloud? The hybrid approach reported herein addresses all these stages of development of warm rain. The calculations improve upon those reported in LCB05 with higher resolution to better represent the entrainment process, and extends them to include calculations of collision and coalescence (with sedimentation), which also follows the growth of the embryos to raindrops within a 3D cloud-model framework. Entrainment is not prescribed directly as was the case in many former studies, but instead results from the dynamical motions of the cloud model. The model framework also allows an evaluation of how prevalent this mechanism might be for accelerating warm rain formation because the embryos follow trajectories derived from their fall velocities and the cloud motions and are not simply assumed to move into regions of high liquid water content. Thus, the question of whether rapid growth of a few of the largest drops due to entrainment and mixing leads to the development of rainfall, in times comparable to those observed in real clouds, is finally addressed in this paper.

2. The model framework

Modeling of the initiation of coalescence requires accurate calculation of the condensation process, which can be compromised unless the size of the bins used for droplet size is very small. The cloud motions that bring about entrainment and associated dilution of the cloud, prominent in all small cumuli, must also be modeled for a reliable comparison.

To represent the collision–coalescence process adequately, another long-standing problem must also be addressed: what are the factors controlling the development of the droplet size distributions in the absence of coalescence? This was the problem addressed in two earlier papers: Cooper (1989) and LCB05. It was argued there that the droplet size distribution at a particular location in a cloud arises from the collocation of an ensemble of droplets that, because of turbulent motions, have experienced variability in their growth conditions before coming together at that point. Those papers suggested that such variability contributes to and perhaps accounts for the observed broadening of droplet size distributions.

LCB05 used the same two-component modeling framework to be used here—a 3D dynamical cloud model coupled with a Lagrangian microphysical model—to develop quantitative predictions of droplet size distributions resulting from entrainment and mixing in small cumulus clouds. The cloud model represented turbulent cloud dynamics with entrainment but parameterized microphysical

processes such as condensation, while the microphysical model performed explicit microphysical calculations that included the activation of cloud condensation nuclei (CCN), condensation or evaporation, and the effects of entrainment and mixing along trajectories constrained to match the thermodynamic and kinematic fields of the cloud model.

The problem of continuing to collision and coalescence and the development of rain was not addressed by LCB05. The new feature of the modeling done in the current study is to add the important next step of collision–coalescence and sedimentation of drops in a novel, albeit in an approximate way, into the model framework, enabling the calculations to be carried forward to the point of formation of the first raindrops. The Lagrangian microphysical model now represents both diffusional and coalescence growth of droplets to raindrop embryos (here taken to be drops larger than $40\ \mu\text{m}$ in diameter). To determine if the embryos produced in the microphysical model can lead to significant rain, they are then allowed to follow their own individual trajectories through the cloud water fields of the 3D cloud model, growing by continuous collection as in the calculations of Lasher-Trapp et al. (2001).

The cloud model used to represent kinematic and thermodynamic properties of the cloud is the Straka Atmospheric Model (Straka and Anderson 1993) as modified by Carpenter et al. (1998), with increased resolution (25 m) from that used in LCB05 to improve the representation of entrainment and small-scale features. This form of the model uses bulk microphysics to represent cloud condensation processes without auto-conversion, because the earliest raindrops are produced explicitly within the microphysical model and later grow by continuous collection in the cloud water field of the cloud model. The cloud model provides a realistic representation of entrainment and provides an estimate of the subgrid-scale turbulence for use in calculations of trajectories and microphysical evolution.

The 1408 UTC 10 August 1995 thermodynamic sounding from the Small Cumulus Microphysics Study (Florida, 1995) was used for the case to be presented. This day was chosen because radar observations showed rapid development of rain in specific times that could be compared to model results and because modeling readily produced high liquid water content (greater than $4\ \text{g m}^{-3}$).¹ As in LCB05, Gaussian heat and moisture

fluxes are inserted at the bottom of the cloud-model domain (located at 4 m MSL) to produce the cloud.

A particular multithermal cloud was studied in SCMS by radar and aircraft. It was about 2 km wide, with cloud base at 730 m MSL, maximum cloud top at 4500 m, and peak radar reflectivity of 40 dBZ. The cloud dissipated about 20 min after its first appearance on radar. The modeled cloud was tuned (via adjustment of the forcing) to have very similar characteristics: multiple thermals up to 2 km wide, cloud-base altitude 725 m, cloud top 4600 m, and about 20-min lifetime before abrupt dissipation (Fig. 1). It exhibits significant variability in the spatial distribution of cloud water as a result of entrainment, as shown in Fig. 2. Significant variability also results in trajectories run backward or forward from any given point in the modeled cloud as a result of the effects of resolved and subgrid-scale turbulence as described by LCB05.

To represent the growth of cloud droplets with the desired accuracy, the Lagrangian or parcel model² discussed by Cooper et al. (1997) and LCB05 was used to represent droplet growth along trajectories in the cloud model. This division into two models was necessary because only the highest-resolution calculations can provide realistic representation of the droplet-growth process. By using bins moving in size in the microphysical model, where each bin corresponds to a specific activation time step at cloud base, it is possible to represent growth by condensation without reassigning droplets to bins. Once coalescence begins, the droplets are reassigned in a way that minimizes computational broadening as described by Cooper et al. (1997). The subgrid-scale turbulence from the simulation was used to calculate the trajectories, but the effects of turbulence on droplet collisions (e.g., Ayala et al. 2008) were not considered in this study.

The appendix documents the details of some changes made to the Lagrangian microphysical model since its description in LCB05 and Cooper et al. (1997). The most significant are these:

- Reactivation of evaporated droplets (e.g., during inhomogeneous evaporation) was incorporated in a straightforward way by using a separate size distribution array, like that for cloud-base CCN, to represent

¹ Study of another cloud with lower liquid water content and smaller lifetime that did not develop precipitation was presented at the Fifteenth International Conference on Cloud Physics in 2008; that study led to selection of this more persistent cloud for the present study.

² This is a parcel model in the sense that a population of droplets formed at cloud base is tracked through the cloud without mixing with the environment except for inclusion of dilution and evaporation as required by entrainment. In reality, mixing of droplets will occur all along such trajectories, usually adding to the variability. The approach taken is a first approximation to the effects of variability in trajectories, but an exact simulation would have to represent mixing of droplets at all times along the trajectories.

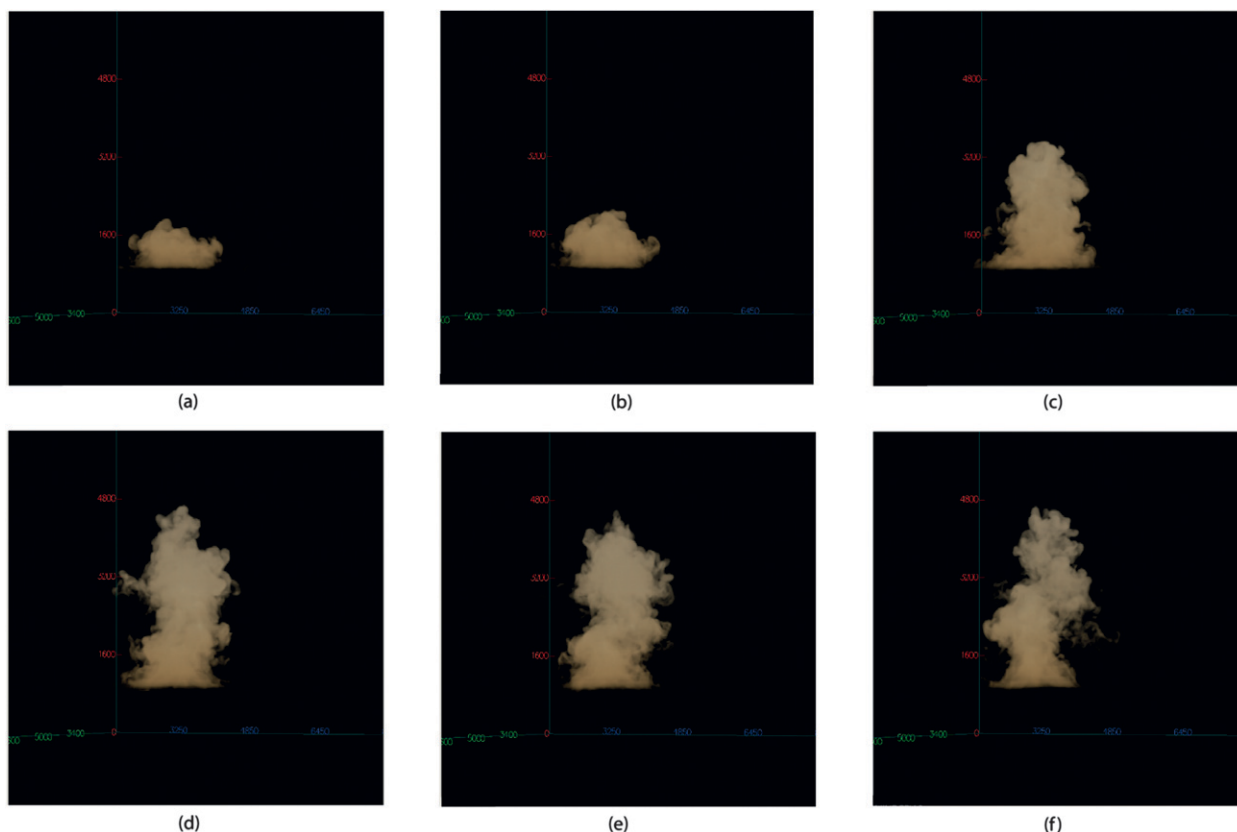


FIG. 1. Time series of photorealistic renderings of a multithermal cloud simulation representative of that occurring on 10 Aug 1995 during the Small Cumulus Microphysics Study. Approximate simulation times are (a) 2, (b) 4, (c) 10, (d) 16, (e) 18, and (f) 21.75 min after the first appearance of the cloud.

both the entrained CCN and those produced by evaporation of droplets. (LCB05 included only initial activation of entrained CCN.) This second array was used to create new droplets when the supersaturation required such activation.

- Several changes were made to the treatment of inhomogeneous evaporation. The basic requirement for inhomogeneous evaporation, from Baker and Latham (1979), is that the time scale for evaporation of droplets be short compared to the time-scale characteristic of the turbulence responsible for the mixing, causing some droplets to evaporate completely while others are unaffected. However, the evaporation times vary with size, so calculations that represent inhomogeneous evaporation should be applied only to those droplets small enough to evaporate on the time scale of the turbulence. It is particularly important to exclude droplets growing on giant CCN if they are too large to evaporate on this time scale, because otherwise the effect of giant nuclei will be underrepresented.
- Recent guidance from the study by Andrejczuk et al. (2006) suggests the specific approach taken here, where

for all calculations the droplet evaporation is considered 50% “homogeneous” and 50% “inhomogeneous.” Their results suggest that mixing proceeds in a nearly universal way for a wide range of mixing proportions, and that for low intensity turbulence (i.e., turbulent kinetic energy less than about $1.6 \times 10^{-4} \text{ m}^2 \text{ s}^{-2}$) the results are approximately midway between the extreme inhomogeneous and fully homogeneous results, with the ratio of the mean droplet concentration to the initial droplet concentration decreasing approximately in proportion to the liquid water content. At higher turbulent kinetic energy, the results are initially characterized by homogeneous evaporation, after which there is a transition to a similar linear behavior. Thus, for each time step, (i) homogeneous evaporation is forced for droplets with evaporation time constants longer than the integral time scale for the turbulence; (ii) for droplets smaller than the threshold defined in the preceding step, the mixing is assumed to lead to 50% homogeneous and 50% inhomogeneous evaporation—specifically, the calculation determines the fraction of droplets that

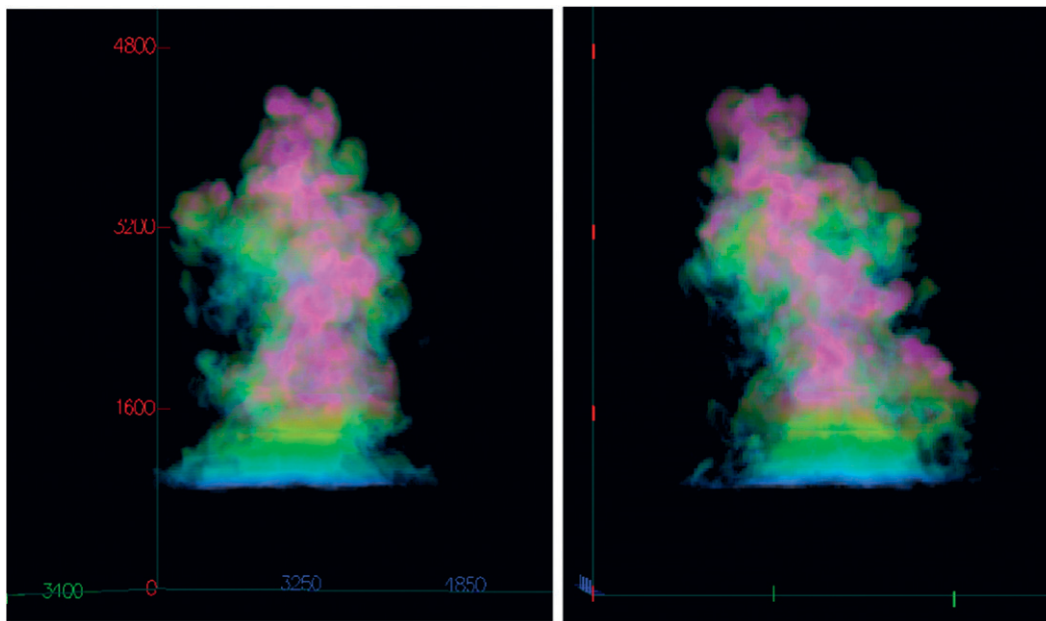


FIG. 2. Renderings [(left) front view; (right) side view] of the same simulated cloud as in Fig. 1, at 14 min after the first appearance of the cloud, showing variability in the cloud water. Color shading indicates ranges of cloud water mixing ratio: dark blue, $0\text{--}1\text{ g kg}^{-1}$; turquoise, $1\text{--}2\text{ g kg}^{-1}$; green, $2\text{--}3\text{ g kg}^{-1}$; yellow, $3\text{--}4\text{ g kg}^{-1}$; and pink, greater than 4 g kg^{-1} .

would evaporate completely to saturate the mixture (as for the extreme inhomogeneous case), but then evaporates only 50% of that fraction of droplets; and (iii) the resulting temperature and vapor pressure are then carried forward so as to drive homogeneous evaporation of the remaining droplets. When the resulting concentration (excluding newly activated droplets produced on entrained CCN) and liquid water content are plotted in the manner of Andrejczuk et al. (2006), the results are quite similar to their universal plots. This and other results suggest that a combination of homogeneous and inhomogeneous evaporation (e.g., Jensen et al. 1985; Lehmann et al. 2009) argue for the realism of this representation of the mixing process. Other choices, investigated but not presented here, do not change the conclusions of this paper.

- The assumed shape of the giant-nucleus portion of the CCN size distribution was changed to reflect better the conditions found in the study location by Lasher-Trapp et al. (2002).

To investigate if large drops produced by entrainment can subsequently encounter regions of high liquid water content and to estimate the amount of rain produced in the cloud, the drops large enough to have significant collection efficiency (i.e., those with diameters greater than $40\text{ }\mu\text{m}$) are inserted into the cloud-model fields and allowed to grow along trajectories in the manner

discussed by Lasher-Trapp et al. (2001). This last step is used to evaluate if the rainfall produced can be considered realistic for a cloud of this type, as discussed in section 4.

3. Typical trajectories

The trajectories followed by the Lagrangian microphysical model were generated as described in LCB05. They were calculated backward in time from a 9×12 horizontal grid of reference points placed 100 m apart. The grid was placed to cover the cloud at 3000 m MSL. To each reference point, (typically) 500 trajectories³ were generated, each leading to the reference point exactly 10 min after the first appearance of the cloud. Of these, 57 reference points were inside the simulated cloud, which at 10 min had just moved through this altitude, and those points form the basis for the calculations

³ Although the goal was to have 500 trajectories reaching a given reference point, in some cases it was only possible to generate half of this number, or even less, especially when the point was near a region of very small liquid water content where most of the air trajectories originated outside the cloud (with the entrained air), rather than in cloudy air that had ascended from the cloud base. Tests showed that the variability was captured well using only 100 trajectories per reference point.

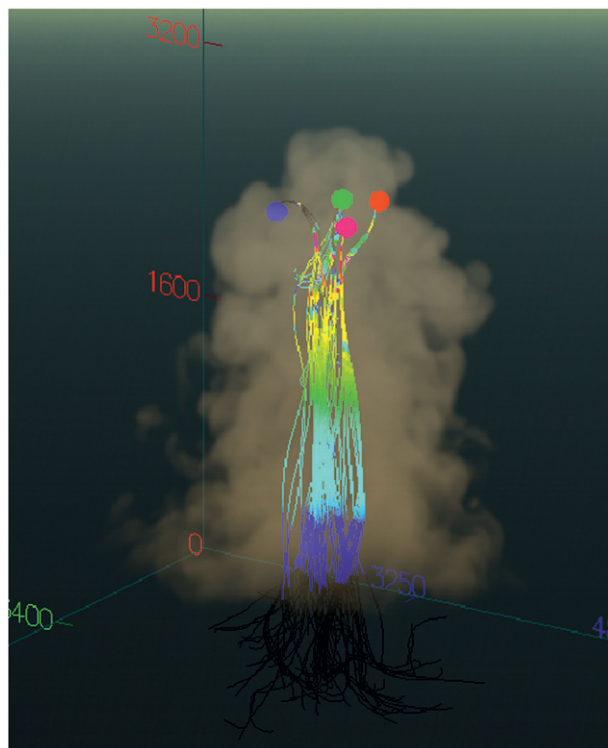


FIG. 3. Photorealistic rendering of the simulated cloud at 10 min after the first appearance of the cloud, overlaid with the entire history of a small subset of the droplet trajectories ascending to four of the reference points. Colors along the trajectories indicate the amount of cloud water at the trajectory location, ranging from dark blue (lowest cloud water) to magenta (highest cloud water content). The labels on the vertical axis are height (m).

that follow. Four of these points are shown in Fig. 3, where some of the variability of the trajectory paths and the influence of entrainment are evident. Loops in the trajectories can arise from the thermal circulation and eddies. Regions of lower cloud water along the trajectories result from entrainment and mixing.

For further illustration, trajectories are picked that originate at cloud base (928 hPa, 22.4°C, and 0.7 km MSL) and rise to 705 hPa, 10°C, and about 3 km MSL. Figures 4a and 4b show some trajectories that arrive at a reference point about 0.6 km from the center of the cloud. Figure 4a illustrates that the trajectories vary significantly in the times when they moved through cloud base: some droplets arriving at the reference point moved through cloud base only 300 s earlier, while others rose for more than 500 s. Figure 4b shows that the wet equivalent potential temperature (Θ_q) history of these droplets also varied significantly: most experienced a rapid decrease from 200 to 100 s before arriving at the reference point, as a result of a significant entrainment event, after undergoing relatively little change before then. However, there are some large departures

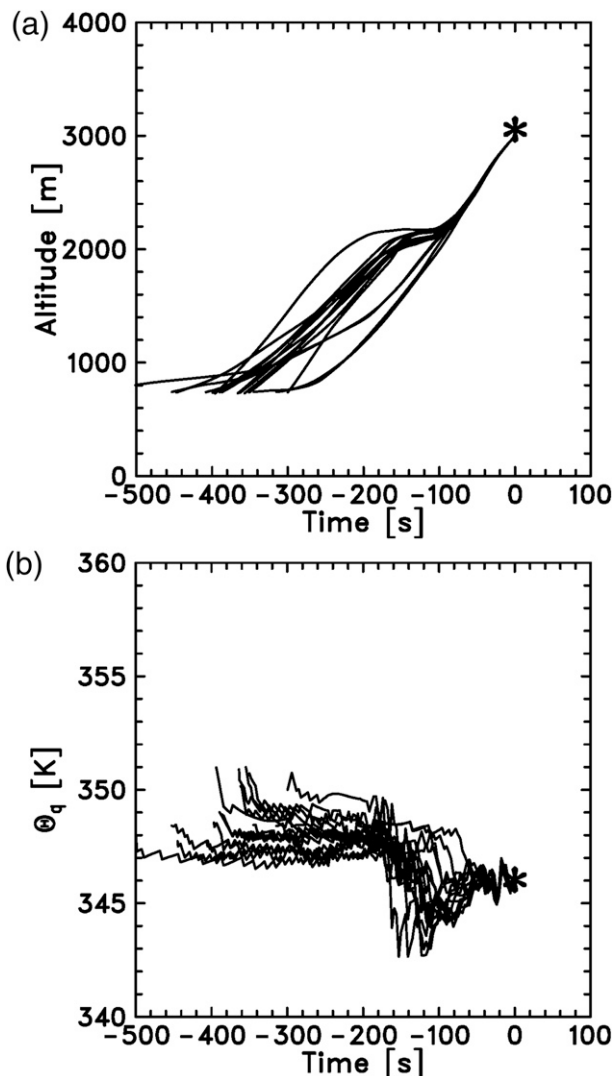


FIG. 4. Examples of (a) ascent rates and (b) Θ_q decreases and increases of individual trajectories that arrive at a reference point (denoted by the large asterisk).

from that mean behavior including some that decrease and subsequently increase in Θ_q . (See discussion of representation of entrainment and mixing in the microphysical model in the appendix for discussion of how such points are handled.) These two plots illustrate that there is substantial variability in the time histories of droplets reaching the reference points, both in available growth time and in thermodynamic properties of the environment.

4. Production of rainfall in the cloud

A droplet size distribution is grown by condensation and quasi-stochastic collision-coalescence along each

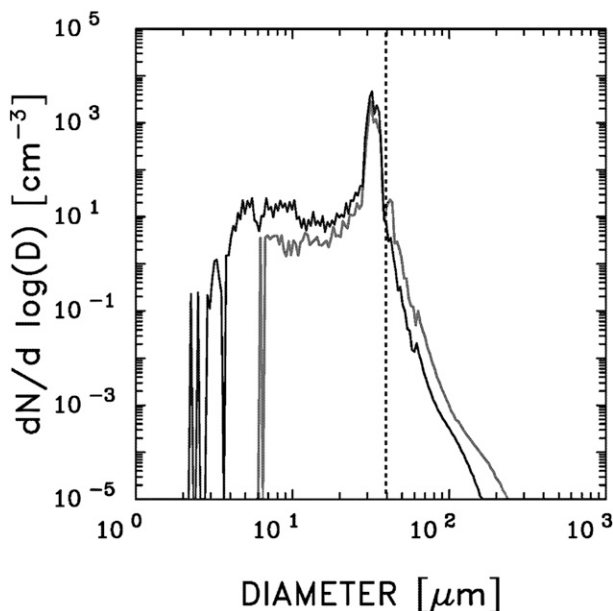


FIG. 5. Droplet size distribution obtained by averaging those from trajectories that reach the reference point (black line). The total droplet concentration was 220 cm^{-3} , liquid water content 3.37 g m^{-3} , and mean diameter $29.4 \text{ } \mu\text{m}$ with standard deviation of $7.0 \text{ } \mu\text{m}$. The new droplet size distribution after 120 s of additional growth to the insertion point, as discussed in the text, is overlaid (gray line). The vertical dashed line denotes a diameter of $40 \text{ } \mu\text{m}$ (see text).

individual trajectory in the microphysical model, but it is the ensemble of these droplet size distributions arriving at any point that must be considered to determine if there is any acceleration of coalescence. To that end, calculations were carried forward from the point of origin of each of the trajectories leading to each of the reference points (cf. section 3). The results at each reference point were then averaged to obtain an estimate of the droplet size distribution present at those points, as in LCB05, with the addition that quasi-stochastic coalescence was also included among the droplets following a given trajectory. This is equivalent, in an averaged sense, to randomly selecting droplets from the ensemble.

An example is shown by the black line in Fig. 5. The mean droplet size distribution included significant large- and small-size portions of the size distribution in addition to the main peak. The distribution is substantially broader than any of the individual distributions, both in terms of the full distribution and in terms of the breadth of the central peak. This size distribution has multiple peaks and substantial breadth toward both smaller and larger droplet sizes and so appears realistic in comparison to size distributions often measured (e.g., Warner 1969).

From each of these reference points, a single trajectory determined from the mean motion in the cloud model was then followed forward for 2 more minutes in the Lagrangian model with explicit microphysics to produce a size distribution such as that shown by the gray line in Fig. 5. The reason for this extension was to allow an opportunity for coalescence to occur in the broadened size distribution. The end point of this 2-min extension will be called the “insertion point” because from there the embryos will be inserted back into the cloud-model fields for continued growth, but following their own trajectories that account for their changing fall speed. This is a compromise forced by the need to perform microphysical calculations with uncompromised accuracy, which in the Lagrangian framework used does not allow consideration of sedimentation, and so must be abandoned once droplets grow to sizes where sedimentation is significant.

The size distribution produced by the various trajectories at a reference point broadens still more as it is carried forward to the insertion point, now just as a result of coalescence. In Fig. 5 the concentration of droplets with diameters greater than $40 \text{ } \mu\text{m}$ is 0.916 cm^{-3} , versus 0.146 cm^{-3} before the additional 2 min of growth. Thus, the calculations show that not only does consideration of the different particle paths, leading later to a single point in the cloud, result in broadening of the cloud droplet size distribution by condensational growth (as shown in LCB05), but also produces raindrop embryos by quasi-stochastic collection enhanced by that broadening. In the next section, the influence of these embryos upon rainfall in the cloud is evaluated.

The amount of cloud water available for collision and coalescence is important at this stage, and thus entrainment and mixing can be a detrimental effect here. Figure 6 shows values of liquid water content between the reference level and the insertion point along a subset of the combined, single trajectories that run from each grid point at the reference level to the insertion points.⁴ For two of these trajectories, the numbers of precipitation embryos are given at the averaging and insertion points. This figure illustrates that while some entrainment and mixing (before 600 s) is important for producing embryos, it can be detrimental to the subsequent production of additional embryos that lead to precipitation if the cloud water decreases too much. Thus, these calculations explain the seemingly contradictory notions of the enhancement of cloud droplet growth as

⁴ The sawtooth pattern evident in some trajectories is simply an artifact of plotting the liquid water content values at a coarser time resolution than was originally used in the cloud simulation.

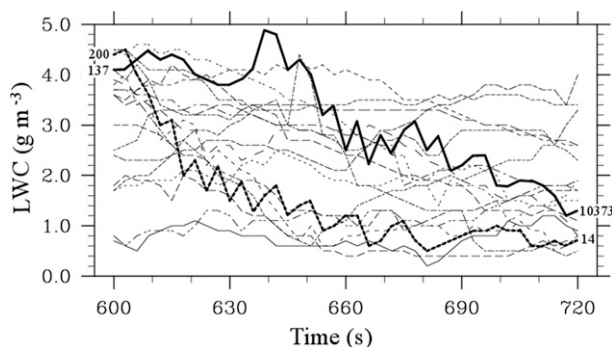


FIG. 6. Time series plot of liquid water content between the reference level (600 s) and the insertion point (720 s), along 19 of the 57 trajectories. Numbers at each end of thick lines denote number of precipitation embryos ($d > 40 \mu\text{m}$) per liter, at those times for those particular trajectories.

a result of entrainment and mixing and the need for substantial cloud water content for collision and coalescence growth as discussed by Twomey (1966) and Jonas and Mason (1982, 1983).

a. Basis for the calculations

To determine if the embryos formed can lead to significant rainfall, the calculations that follow evaluated the growth of those embryos by inserting them into the cloud water fields of the cloud model. Lasher-Trapp et al. (2001) described the approach, which is continuous collection with consideration of collection efficiencies for the parameterized size distributions of the collected cloud water. Up to the insertion points, fall speeds of the droplets were neglected when determining trajectories because the fall speed of a droplet $40 \mu\text{m}$ in diameter is only about 5 cm s^{-1} (Beard 1976)—negligible compared to the cloud simulation velocities. However, for embryos growing to raindrops, fall speeds become comparable in magnitude to air motions in the cloud, so the calculated drop trajectories through the cloud must then take into account the size and fall speed of individual drops as well as the air motions in the cloud.

The calculated collection growth by the embryos continued until the liquid water content of the model cloud became depleted at the end of the cloud lifetime (cf. Fig. 1f), about 10 min after the insertion time. Because the total precipitation mass remained a small part of the cloud water, no feedback was needed to represent either depletion of the cloud water by this growth or possible dynamical effects on the cloud model. The size distributions that resulted at the end of these calculations then form the basis for the estimates of rainfall, rain rate, and precipitation efficiency that follow.

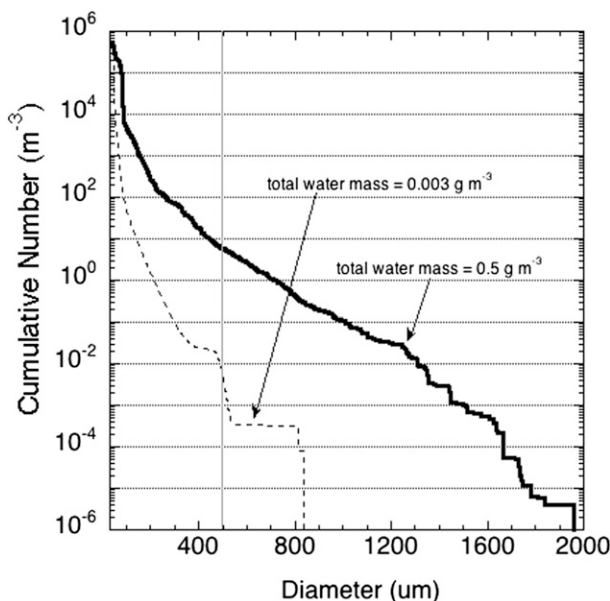


FIG. 7. Cumulative drop size distribution averaged over all 57 insertion points for embryos produced in the microphysical model (dashed line), and at the end of the continuous collection calculations (solid line). The final size distribution includes all drops located anywhere in the cloud along their respective trajectories, as if returned to their initial collocated concentration at insertion time. Vertical line at $500\text{-}\mu\text{m}$ diameter is shown as a reference value, as discussed in the text.

b. Resulting drop size distributions

Figure 7 shows the average size distribution of the embryos at the 57 insertion points and the final sizes after nearly 10 min of additional growth by continuous collection of cloud water. The average cumulative size distribution of all the initial embryos at the insertion points shows that over 0.5 cm^{-3} drops with diameters of $40 \mu\text{m}$ and larger were inserted into the continuous collection model, and nearly 6 m^{-3} of these exceeded $500 \mu\text{m}$ in diameter at the end of the calculations. The amount of water mass contained in the precipitation embryos, initially only 0.003 g m^{-3} , grew to 0.5 g m^{-3} after 10 additional minutes of growth (where the units refer to the mass that would be present if the raindrops, now distributed through the cloud as a result of their different fall speeds, were returned to the original volume of air at the insertion point). The instantaneous rain rate, calculated by averaging the results at the 57 insertion points, was 2 mm h^{-1} . Tests with two other reference grids (entirely different sets of trajectories run up to higher and lower altitudes at times 2 min earlier and later than the reference grid used here), produced higher rain-rate values, with a maximum of about 6 mm h^{-1} .

To check that the minimum size used for embryos was adequate, the calculations were repeated with embryo

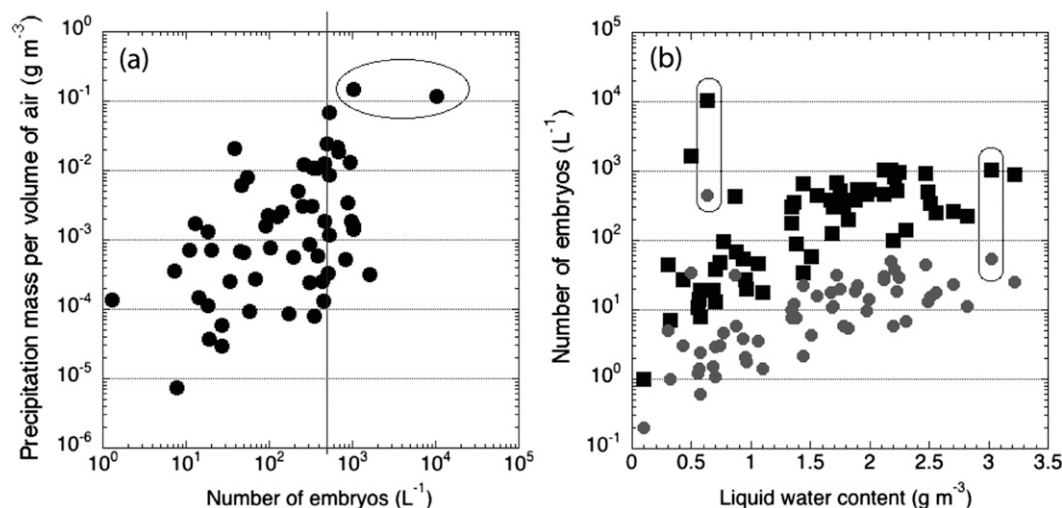


FIG. 8. For all insertion points in the cloud, (a) number of embryos exceeding $40\text{-}\mu\text{m}$ diameter produced at each point vs the precipitation mass (for drops exceeding $200\text{-}\mu\text{m}$ diameter) attributable to those embryos, and (b) the initial cloud water content at a given point vs the number of embryos exceeding either 40 (squares) or 50 (circles) μm in diameter at that point. Points lying within ovals are discussed in the text, and the vertical line in (a) separates points having in excess of 0.5 cm^{-3} or 500 L^{-1} embryos.

sizes of 30- , 40- , and $60\text{-}\mu\text{m}$ diameter. The result was that the contribution from droplets smaller than $40\text{-}\mu\text{m}$ diameter was negligible, so this choice includes essentially all the rain production. At the time when the continuous collection calculations were halted, the largest embryos had fallen beneath the cloud base, those in the middle of the range had fallen through most of the cloud, but the smallest embryos were still in the upper parts of the cloud, not far from where they were released. The small fall speeds and collection efficiencies of such drops prevent their growth in a continuous-collection calculation such as this. It is a weakness of the calculations presented here and is likely to result in an underestimate of the rainfall, because it does not permit collisions among the embryos that might stochastically produce larger drops with larger fall speeds and collection efficiencies.

A consistent result among numerous runs with the modeling framework, including results from a cloud simulation different from that shown here and results with different times and locations for insertion points in the simulated cloud, is that the number of embryos produced by the variability in supersaturation histories resulting from entrainment and mixing in a region of the cloud is not a good predictor of the amount of precipitation that eventually will result from such embryos. As shown in Fig. 8a, a given number of embryos could later produce a precipitation mass that ranges over two orders of magnitude. Although there were more than 0.5 cm^{-3} embryos at numerous insertion points (vertical line in Fig. 8a), some grew little by collection of cloud

water as they fell through the cloud, while others grew much more. The greatest numbers of embryos often resulted from strong entrainment events, but the embryos could reside in regions of small liquid water content, at least initially (Fig. 8b), limiting further growth by collection. Small and Chuang (2008) reported similar findings in trade wind cumuli: the largest drops were present near the cloud top in regions of reduced liquid water content.

Thus, similar amounts of precipitation can result from different numbers of embryos at a given point, depending upon if they can be reintroduced into regions of greater cloud water. The circled points in Fig. 8a produced nearly equivalent precipitation masses although one point had an order of magnitude more embryos than the other. These same two points are circled in Fig. 8b, which shows that the point with the smaller number of embryos initially resided in a region of much greater cloud water where the embryos could grow to larger sizes more quickly than the point with the greater number of embryos residing in a region of less cloud water. At least some of those embryos encountered a region of greater cloud water at some point in order to produce such a precipitation water content. Here too, then, the limiting effect of entrainment on precipitation development is clear. While some entrainment can be useful in producing a broad size distribution of droplets that favor collision-coalescence growth, the larger droplets thus formed can only be useful if immersed in sufficient cloud water for collection to form raindrops. Thus, this study reinforces the argument of the need for substantial liquid

water for precipitation formation as discussed by Twomey (1966), for example.

The scatter in these plots also demonstrates another tendency in the results: a small number of preferred locations produced the majority of the initial precipitation. Three points were responsible for 61% of the total precipitation mass created among this set of 57 insertion points. These results suggest that the majority of the earliest raindrops are produced in a few rare regions within a cumulus cloud, as would be consistent with the difficulty in finding them with in situ cloud observations (e.g., Beard and Ochs 1993, Small and Chuang 2008, and references therein).

c. Estimated rainfall

For use in extrapolating the results over the lifetime of the cloud, the mass flux of precipitation M and rain-rate R were calculated from all of the drops larger than 100- μm diameter, located anywhere in the cloud at the time the continuous collection model is halted, from

$$R = \frac{M}{\rho_w} = \frac{1}{\rho_w} \sum_i n_i m_i v_i, \quad (1)$$

where n_i , m_i , and v_i are respectively the number concentration, mass, and fall speed of drops in each size class i and ρ_w is the density of water. The mass flux and rain rate, in this particular case equivalent to 1644 kg s^{-1} and 2 mm h^{-1} , respectively, then represent quantities resulting from the embryos at the insertion time.

These drops, however, are replaced by others as the air motions bring new condensate to this level. If, for example, a 5 m s^{-1} updraft is present at a given 25-m grid box, the full grid box at that altitude is replaced every 5 s, so the resulting rain rate seen throughout the cloud receives an independent contribution from this grid box each 5 s. The total precipitation from this grid box is then related to the cumulative mass flux, if all the precipitating mass remains in the cloud.

If it is assumed that the condensate has negligible fall speed in comparison to the updraft speed, the condensate flux through the reference level is $F = \chi w$ where χ is the liquid water content and w (a function of time) is the updraft speed from the cloud model at each grid point at the reference level height of 3000 m. A precipitation efficiency can then be determined by the ratio $\epsilon = M/F$. This is an unconventional definition of precipitation efficiency because the precipitating mass flux is calculated from the fall velocities rather than relative to a ground-referenced coordinate system. At the reference level and time, F obtained in this way is 7926 kg s^{-1} , yielding a precipitation efficiency of 21%. Estimates of similar magnitude have been documented for deeper

cumulonimbi based on observations (e.g., Fankhauser 1988) and numerical modeling (e.g., Ferrier et al. 1996).

If all precipitation so formed eventually reaches the ground and all precipitation forms from drops passing through the reference level at 3000 m MSL, the total rainfall can be estimated from $T = \int \epsilon(t) F(t) dt$. Because about 30 000 trajectories were used to estimate the rainfall at a single time, repeating such calculations at regular intervals throughout the cloud lifetime was impractical. Instead, an approximate measure T_e was obtained by assuming that the precipitation efficiency remained constant: $T_e = \epsilon_0 \int F(t) dt$, where ϵ_0 is the precipitation efficiency calculated at the reference level and time. For this estimate, the time integral extends from when condensate first reached the reference level until the condensate flux decreased to 66% of its peak value at that level: a period of 7.5 min. Values of F were computed at the reference level from the simulated cloud in 30-s intervals. The lifetime rainfall was approximately 0.4 mm averaged over the insertion points (which covered a total area of about 0.6 km^2), leading to a total rain mass of about 2.4×10^5 kg. This is a small amount of rainfall, but the significance of this result is that it was initiated in less than 20 min—a result that has been difficult to achieve in realistic simulations of the development of warm rain.

5. Sensitivity to some factors that influence the formation of rain

a. Giant nuclei

Both in observations of some small cumulus clouds (Caylor and Illingworth 1987; Illingworth 1988; Knight et al. 2002) and in these calculations, giant nuclei play a significant role in the early development of precipitation, especially in the formation of the largest drops. The concentration used for such nuclei in this study is based on the estimates of (Lasher-Trapp et al. 2002), which are lower than the estimates for generation from the sea surface under high-wind conditions (Johnson 1982; Woodcock 1952, 1953, 1978; Woodcock et al. 1971), but are appropriate for low to moderate wind, as argued in the appendix. The sensitivity study here suffers from the poor representation of the growth of the larger droplets formed on giant nuclei, arising from the neglect of the fall speed of such drops prior to the insertion point. Thus, the giant aerosol travel to higher levels of the cloud and encounter regions of greater liquid water content than they would have if their sedimentation were considered immediately, as it should be, and as was done in Lasher-Trapp et al. (2001). Hence, this sensitivity study is intended only to determine if

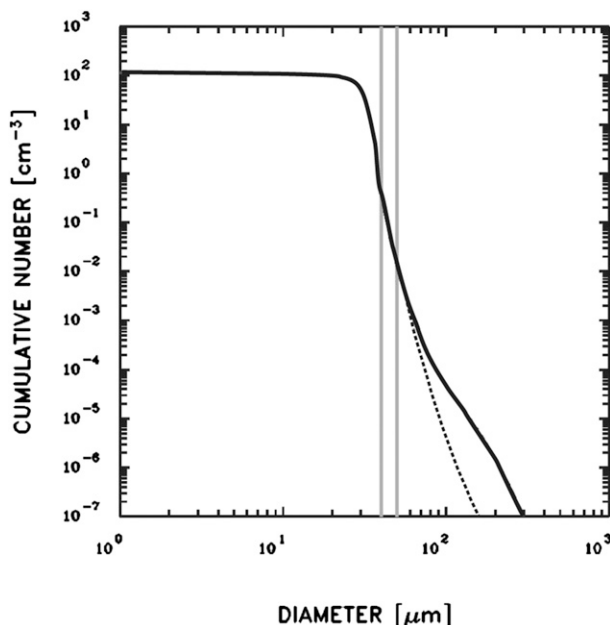


FIG. 9. Cumulative drop size distribution for the standard calculations (thick line) and for a test calculation (dotted line) for which all CCN with dry diameter exceeding $2\text{ }\mu\text{m}$ in diameter were eliminated from the input CCN size distribution. The vertical gray lines denote 40- and $50\text{-}\mu\text{m}$ diameters—limits used in the text for measures of embryo production.

such nuclei completely dominate the rain-formation process in the results reported here.

To determine the influence of the assumed concentration of giant nuclei in these results, those nuclei larger than $2.0\text{ }\mu\text{m}$ in diameter were eliminated from the assumed CCN distribution and the calculations leading to rain were repeated. Figure 9 shows the resulting cumulative drop size distribution averaged for all the size distributions at the insertion points. The giant nuclei account for the difference at largest sizes, but there is little difference for the total concentrations of embryos exceeding 40 and $50\text{ }\mu\text{m}$ in diameter (Table 1). However, the giant nuclei still have a strong influence on the initial formation of rain in these calculations. The rain rate, total rainfall, and precipitation efficiency produced in the calculation without giant nuclei were far less (Table 1). While the number of drizzle-size drops is dominated by coalescence growth from the main peak, the giant nuclei still account for a majority of the rainfall that develops in this modeled cloud. In subsequent development of precipitation in longer-lived clouds, the continued presence of drizzle will contribute to precipitation development, but the larger drops developing from the giant nuclei may also shatter into smaller drops either spontaneously or as the result of collisions, so it is difficult from these calculations to estimate the relative

TABLE 1. Concentration of precipitation embryos larger than $40\text{ }\mu\text{m}$ (E_{40}) and $50\text{ }\mu\text{m}$ (E_{50}), resulting rain rate, total rainfall, and precipitation efficiency (PE) for the three model runs.

Model run	E_{40} (L^{-1})	E_{50} (L^{-1})	Rain rate (mm h^{-1})	Total rainfall (mm)	PE %
Standard	0.330	0.0135	1.9	0.4	21
No GA	0.317	0.0113	0.7	0.1	8
Single traj	0.126	0.0075	1.1	0.2	13

importance of the two sources of raindrop embryos over the life cycle of such a cloud. There are also other effects not explored here that can increase the production of drizzle via collisions in the main peak of the droplet size distribution, especially the effects of turbulence on collision efficiencies and rates, that would compete with the growth on giant nuclei.

b. Broadening of the droplet size distribution by variability in trajectories

To assess the importance of the broadening of the droplet size distribution that occurs from variability in the supersaturation histories among trajectories reaching a specified point in the cloud, the calculations presented earlier were repeated using only a single trajectory from cloud base to each insertion point. These trajectories still passed through the reference points in the cloud, but no mixing of different trajectories occurred there. In this test calculation, entrainment and mixing still affected the droplet size distribution as required to match cloud conditions along the selected droplet trajectory, but there was no broadening caused by mixing together of droplets following different trajectories up to the reference point, as shown to occur in LCB05. The result is shown in Table 1. There was considerable variability among the single trajectories that could be selected for this example, but the typical result was that a single trajectory leads to a much narrower droplet size distribution than the ensemble-average result and leads to fewer total embryos larger than either 40- or $50\text{-}\mu\text{m}$ diameter (Table 1), and thus about half as large a rain rate and total rainfall as the ensemble-average runs. This illustrates that the additional rainfall produced by coalescence in the modal peak of the droplet size distribution arises (in this particular cloud) because of broadening of that main peak via the mechanism of mixing of different droplets with different growth histories as a result of entrainment and mixing.

c. Variability arising near cloud base

The trajectories reaching a given location in the cloud originate from various locations at cloud base where updrafts vary, so this variability will contribute to

broadening of the droplet size distribution [e.g., the arguments in Cooper (1989)]. To estimate the importance of this contribution, calculations were repeated for which entrainment along the trajectories was suppressed. These trajectories duplicated the actual ascent times of entraining parcels in order to include realistic times for broadening by coalescence. The mean droplet size of a representative set of 500 trajectories leading to a single point at the reference level was $30.29\ \mu\text{m}$ and the standard deviation was $0.84\ \mu\text{m}$, while for the same trajectories the standard calculation with entrainment produced approximately the same mean size but gave a standard deviation of $4.33\ \mu\text{m}$. True adiabatic ascent produced a standard deviation of about $0.30\ \mu\text{m}$, so variability at cloud base does make a small contribution to the width of the droplet size distribution, but the dominant effect arises from variability in entrainment and mixing as discussed in the previous section.

6. Summary and conclusions

The calculations presented here have shown that the mixing together of droplets having variability in their growth histories, all resulting from entrainment and mixing, can indeed be important for the earliest warm rain formation. This mechanism has been presented and studied extensively in past studies, but a lack of consideration of the time-evolving, three-dimensional structure of a cumulus cloud have limited the strength of those arguments. The hybrid modeling framework used here combines a high-resolution 3D cloud model that has a realistic representation of entrainment, with a parcel model in which highly accurate calculations of the evolution of the droplet size distributions via condensation and stochastic coalescence are performed.

The results also verified the apparent contradiction that although entrainment reduces the liquid water content in the cloud, it can also broaden the droplet size distribution in ways that aid the formation of warm rain, when rain-drop embryos resulting from collision-coalescence among a droplet spectrum broadened by entrainment and mixing move into areas of greater liquid water content that maximize their subsequent growth by collection. The present study has shown that while these occurrences are relatively few, they can occur, and produce the bulk of the first rainfall.

The influence of giant nuclei was large in the formation of the first rainfall in this modeled cloud, and competes with the importance of the main rain formation mechanism presented here. However, their importance might be overestimated owing to the neglect of sedimentation in the early stages of the calculations, and thus a more thorough study addressing this limitation,

and of their relative influence under different environmental conditions, is warranted.

In the cloud studied, a small amount of rain formed via collision-coalescence in less than 20 min. This value is likely a conservative estimate, because of the neglect of quasi-stochastic coalescence among the raindrops after they are inserted into the continuous collection model. However, the calculated rainfall is appropriate for the initial rainfall from a small cumulus cloud as observed during the SCMS, albeit in the lower range. This was the goal of the paper. Some SCMS clouds that produced more rain likely had a different dynamical evolution than the cloud modeled here, so a one-to-one comparison with a specific SCMS case is not possible.

Many other factors can influence the initiation of coalescence, including the effects of turbulence, history of the liquid water content in the cloud, aerosol concentration, suppression of diffusional growth by surfactants, use of different collision efficiencies, and different assumptions regarding the nature of the mixing. These factors can be explored more fully using the framework developed in this paper.

Acknowledgments. The National Center for Atmospheric Research (NCAR) is sponsored by the National Science Foundation (NSF). Support for the second author was provided by the NSF Grant ATM-0342421 and for the third author from the Natural Environment Research Council (NERC) Grant NER/A/S/2003/00360. Most of the numerical modeling for this study was conducted on the supercomputers of the Computational and Information Systems Laboratory at NCAR. Photorealistic renderings of the cloud simulation and associated trajectories were made with software developed under NSF Grant IIS-0513464 in collaboration with Dr. D. Ebert of Purdue University.

APPENDIX

Changes to the Microphysical Model

a. Treatment of inhomogeneous evaporation

Equation (3) from LCB05 provides an estimate of the integral time scale of the subgrid-scale turbulence, and Eq. (3) from Cooper (1989) provides a similar estimate of the evaporation time, so these times are now compared and inhomogeneous evaporation is suppressed for drop sizes larger than the size for which these times are equal. This process uses the turbulent kinetic energy from the dynamical model and the drop size in the Lagrangian microphysical model to make the comparison. Including

this transition avoids unrealistic evaporation of, for example, growing drizzle-size drops that are important embryos for the formation of rain.

An error was found and corrected in the representation of inhomogeneous evaporation as used in LCB05. The drop concentration for all bins was reduced as appropriate for mixing, then the liquid water content was calculated for the parcel, but the resulting water content was then erroneously reduced again for dilution. This led to an overestimate of the effect of inhomogeneous evaporation, which has now been corrected. (LCB05 used an adjustable parameter to scale the results between fully homogeneous and fully inhomogeneous evaporation, so this error is equivalent to having more inhomogeneous evaporation than characterized by that adjustable parameter, by typically about a factor of 2.) This error does not change the conclusions of LCB05.

The following provides the detailed manner in which this scheme is implemented:

- 1) Find the mixing fraction F of environmental air, with equivalent wet-bulb potential temperature Θ_q^E , in a unit of mixed air needed so that Θ_q^P of the resulting air parcel will match that of the cloud model Θ_q^C :

$$F = \frac{\Theta_q^P - \Theta_q^C}{\Theta_q^P - \Theta_q^E}. \quad (\text{A1})$$

To make the transition gradual, if $F > 0.1$, force $F = 0.1$ to provide a slower relaxation to the cloud-model values at each time step.

- 2) Adjust the parcel properties:
 - (i) Adjust Θ_q of the parcel: $\Theta_q^P \leftarrow \Theta_q^P(1 - F) + F\Theta_q^E$. For F as in (A1), this sets the air-parcel equivalent wet-bulb potential temperature to the cloud-model value; otherwise, this moves the parcel value toward the cloud-model value.
 - (ii) Adjust parcel humidity variables (mixing ratio r and total-water mixing ratio r_t) in the same proportions. This step results in a new supersaturation, after the new temperature is calculated, and the condensation/evaporation process will then continue as a natural part of ensuing calculations.
 - (iii) Dilute the (unactivated) entrained-CCN size distribution in the parcel by the factor $(1 - F)$, then add $F n_{\text{CCN}}^E$ where n_{CCN}^E is the size distribution of CCN in the near-cloud environment.
- 3) Branch on evaporation type:
 - (i) Homogeneous evaporation: dilute the drop concentration, including any formed on entrained CCN, by $(1 - F)$;

- (ii) Inhomogeneous evaporation, fraction f_{IH} ($0 < f_{\text{IH}} \leq 1$)

- Find the portion of entrained air F' that must mix with a portion $(1 - F')$ of air from the cloud parcel to produce a just-saturated mixture. The portion F' is different from F ; indeed, the wet equivalent potential temperature of this initial saturated mixture Θ_q^* will generally differ from the final mixture, and the portion of the cloud drops not evaporated may remain in a supersaturated or subsaturated environment:

$$\Theta_q^* = (1 - F')\Theta_q^P + F'\Theta_q^E, \quad (\text{A2})$$

$$r_t^* = (1 - F')r_t^P + F'r_t^E. \quad (\text{A3})$$

If the result is to be just saturated, then the total-water mixing ratio must satisfy

$$r_t^* = \frac{\varepsilon e_s(T^*)}{p - e_s(T^*)}, \quad (\text{A4})$$

where $e_s(T^*)$ is the saturation vapor pressure at temperature T^* . The temperature of the intermediate just-saturated parcel T^* is then adjusted iteratively to satisfy the constraints (A2)–(A4).

- Determine the fraction of drops β that must be evaporated completely to produce the saturated final mixture. This is related to the fraction of entrained air according to

$$\beta = F \frac{1 - F'}{F'(1 - F)}. \quad (\text{A5})$$

The value of β is then multiplied by f_{IH} to cause only that fraction of the water required to saturate the mixture to evaporate inhomogeneously. This makes it possible to vary the nature of the evaporation from pure homogeneous to pure inhomogeneous by varying the variable f_{IH} .

- Remove the fraction $f_{\text{IH}}\beta$ of cloud drops from the size distribution and add this amount of water, evaporated, to the vapor pressure of the resulting mixture. However, limit the evaporation of large drops, as described above.
- Dilute the resulting drop concentration as required by the addition of environmental air. In terms of the preceding variables, this requires that the drop concentration be multiplied by

$(1 - F)(1 - f_{\text{IH}}\beta)$ for all drops for which inhomogeneous evaporation is indicated, and by $(1 - F)$ for all large drops for which homogeneous evaporation should apply.

- Adjust the number of unactivated CCN to include the remnants from the evaporated drops.

b. Increases in Θ_q along parcel trajectories

Another source of some criticism and discussion of LCB05 was the manner in which droplets were treated in the Lagrangian microphysical model when the wet equivalent potential temperature Θ_q increased along the trajectory. Figure 4 shows some such trajectories. To address this, three options were tested: (i) force a constant value of Θ_q when the model requires Θ_q to increase; (ii) impose a floor, so that a parcel never drops below the final Θ_q of the trajectory, avoiding unrealistically low values resulting when low values were encountered followed by subsequent increases to the final point; (iii) allow entrainment in a negative sense—that is, remove environmental air from the parcel to increase its value of Θ_q to match that of the cloud model. By comparing results with these assumptions, it is possible to judge the uncertainty introduced by weakness in the representation of such processes.

The results presented in this paper are based on (iii). Other choices led to different droplet size distributions but did not change the basic conclusions of this paper. To illustrate the sensitivity to this choice, calculations to a specified reference point were made using each of these assumptions. The standard results for this point had 1.041 cm^{-3} embryos larger than $40 \mu\text{m}$ and 0.0300 cm^{-3} larger than $50 \mu\text{m}$ in diameter developed by the insertion point. In contrast, for options (i) and (ii), the corresponding results were 0.544 and 0.787 cm^{-3} embryos larger than $40 \mu\text{m}$ and 0.0157 and 0.0185 cm^{-3} larger than $50 \mu\text{m}$. Either of these choices decreased the production of drizzle relative to the choice made in the present study by amounts of about 50% or 25%, respectively. Choice (i) seems unrealistic because it tends to force the final parcel to be too dilute relative to the cloud model. However, (ii) and (iii) should provide limits to the true effects, so this comparison and other similar ones suggest that the uncertainty associated with this choice is on the order of 25% or less.

c. The CCN size distribution

Some questions have arisen in connection with the definition of the cumulative CCN supersaturation distribution as used in Cooper et al. (1997), so that definition is documented in more detail here. Changes are also

imposed because it appeared that the distribution as used there included an unreasonable contribution at very large sizes (greater than $25\text{-}\mu\text{m}$ diameter), so the representation was changed to make it possible to eliminate these very large CCN while still providing a complete size distribution of the particles assumed to be CCN. As in LCB05, we assume the CCN to be soluble and composed of ammonium sulfate.

We follow standard references (e.g., Pruppacher and Klett 1997) to obtain the critical saturation ratio for activation in terms of the dry particle size:

$$\ln S_c = \frac{C^*}{r_s^{3/2}}, \quad (\text{A6})$$

where

$$C^* = \frac{2A^{3/2}}{(27B)^{1/2}(4\pi\rho_s/3)^{1/2}},$$

$$A = 2\sigma M_w / \rho_s RT,$$

$$B = 3iM_w / 4\pi\rho_s M_s,$$

and S_c is the critical saturation ratio for activation of the CCN [at critical supersaturation SS such that $S_c = 1 + (\text{SS}/100\%)$], ρ_s the density of the soluble particle, σ the surface tension of the solution droplet, M_w the molecular weight of water, R the universal gas constant, T the temperature of the solution droplet, and i the van't Hoff factor for the salt in solution.

If the differential distribution functions associated with the cumulative distribution functions $n(\text{SS})$ and $N(r_s)$ are, respectively, $f(\text{SS})$ and $F(r_s)$, and if $\text{SS}/(100\%)$ is small compared to unity, then

$$\frac{\text{SS}}{100\%} \approx C^* r_s^{-3/2}$$

gives the relationship between critical supersaturation SS and the size of the particle r_s . Then, from $F(r)dr = -f(\text{SS})d\text{SS}$,

$$F(r_s) = -Ck(100\text{SS})^{k-1} \frac{d\text{SS}}{dr_s}$$

or

$$F(r) = C' r^\alpha, \quad (\text{A7})$$

where $C' = 1.5Ck(100C^*)^k$ and $\alpha = -(3/2)(k-1) - (5/2) = -(3/2)k - 1$. Equation (A7) then specifies the size distribution in terms of the parameters of the CCN spectrum.

The total mass of the size distribution is

$$M = \int F(r_s) \frac{4}{3} \pi r_s^3 \rho_s dr_s \sim r_s^{4+\alpha},$$

so, to avoid having the large-size part of the distribution contribute an infinite mass, it is necessary that α be smaller than -4 . This requires $k > 2$, which is a condition seldom met by measured CCN spectra. For this reason, it is necessary to combine the CCN spectrum with one at large sizes that has a steeper decreasing slope with size. One candidate is the Junge cumulative size distribution $N_J(r_s)$, suggested as valid for sizes larger than radii of $r_1 = 0.1 \mu\text{m}$ and specified as

$$\frac{dN_J(r_s)}{d \log_{10}(r_s)} = \frac{A_J}{r_s^3}, \quad (\text{A8})$$

where $A_J = 10^{-13}$. In this form, A_J is dimensionless. The differential size distribution $F_J(r_s) = dN_J(r_s)/dr_s$ is then

$$F_J(r_s) = \frac{A_J}{\ln(10)r_s^4}. \quad (\text{A9})$$

A property of the Junge size distribution is that all logarithmic intervals contribute equally to the mass, so again some truncation or modification is needed at large size. If the upper limit to this size distribution is taken to be r_2 , the concentration between radii r_1 and r_2 becomes

$$\int F_J(r_s) dr_s = \frac{A_J}{3 \ln(10)} \left(\frac{1}{r_1^3} - \frac{1}{r_2^3} \right). \quad (\text{A10})$$

At the largest sizes, the evidence presented by Alofs and Liu (1981) argues for a steeper descent, for which $dN_A(r_s)/d \log_{10} r_s = A_A r_s^{-\beta}$ with $\beta = 4$. This provides the desired result of having a full size distribution function with finite mass at the largest sizes. A transition to this might reasonably be made at a radius of $r_2 = 1 \mu\text{m}$.

The following is the procedure used to match these distributions at the transition sizes:

- (a) First, consider the transition from the Junge region to the largest-size region, assumed to occur at r_J . If $N_A(r_s) \sim r_s^{1-\beta}$ and $dN_A/d \log_{10} r_s = A_A r_s^{-\beta}$, so to match to the Junge distribution at $r_s = r_J$ it is necessary that

$$\frac{dN_J}{d \log r_s} = \frac{dN_A}{d \log r_s}$$

or

$$\frac{A_J}{r_J^3} = \frac{A_A}{r_J^\beta}$$

so

$$A_A = A_J r_J^{\beta-3}. \quad (\text{A11})$$

The cumulative number of CCN with sizes larger than r_s in the largest-size region, for $r_s > r_A$, is then

$$N_A(r_s) = A_A \frac{\beta}{\ln(10)} r_s^{-\beta}. \quad (\text{A12})$$

- (b) For the transition from the small-size region specified as $C(\text{SS}/100)^k$ to the Junge distribution, the size at which the transition occurs is specified as $r_t = 0.1 \mu\text{m}$ radius. Then, with the slope specified for the Junge distribution, the concentration is adjusted to match that from the small-CCN distribution at that size. This gives a continuous cumulative size distribution function, although there is a discontinuity in the differential size distribution. This has not produced an apparent gap in the initialized size distribution.

The Junge integral then gives a cumulative number from r_t upward of $A_J/[3 \ln(10)r_t^3]$. The corresponding supersaturation is $\text{SS}/100 = C^* r_t^{-3/2}$ so matching the cumulative distribution functions gives

$$\text{CC}^* k r_t^{-3k/2} = \frac{A_J}{3 \ln(10)r_t^3}$$

or

$$A_J = 3 \ln(10) \text{CC}^* k r_t^{3-3k/2}. \quad (\text{A13})$$

The size distribution is then specified by the parameters C and k of the small-size distribution function, the lower and upper limits (r_1, r_2) for which to use the Junge distribution, and the power-law dependence β assumed for the largest sizes. In addition, a cutoff size is imposed to avoid some of the largest ultragiant aerosols. For the calculations presented in this paper, the choices were $C = 365 \text{ cm}^{-3}$, $k = 0.23$, Junge lower and upper limits of 0.2- and 2- μm diameter, and a power-law dependence as $\beta = 4$ as specified above. The ultragiant aerosol population was also truncated at a diameter of 50 μm , but tests with this truncation extended to 1000 μm showed negligible effect on the rainfall. The corresponding cumulative size distribution for CCN composed of ammonium sulfate is shown in Fig. A1. This figure is reasonably consistent with the summary figure of previous observations presented by Jensen and Lee (2008, their Fig. 1), except at the highest

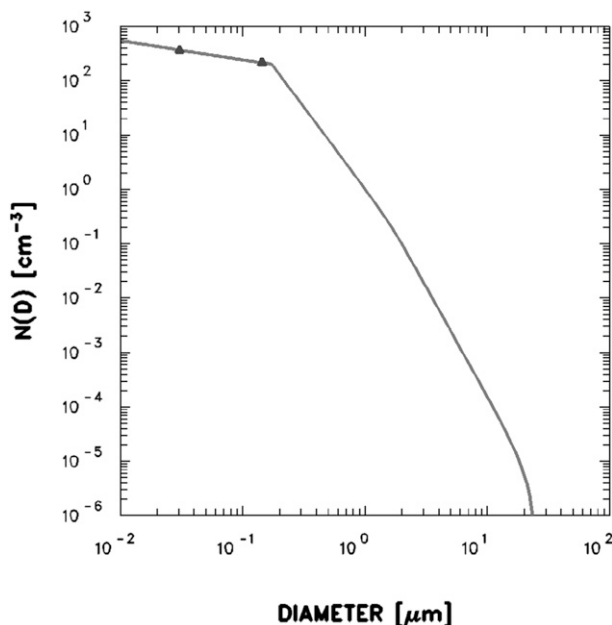


FIG. A1. Cumulative aerosol size distribution used in this study. Two dots denote the 0.1% and 1% critical supersaturation points. The size distribution is truncated to eliminate ultragiant nuclei with diameters larger than 25 μm .

wind speeds where it would underestimate the giant-nucleus concentration.

For entrained CCN, there is little basis for a choice. The assumption was made that entrained CCN are similar in size distribution but have a concentration half as large as the CCN entering through cloud base.

REFERENCES

- Alofs, D. J., and T. H. Liu, 1981: Atmospheric measurements of CCN in the supersaturation range 0.013–0.681%. *J. Atmos. Sci.*, **38**, 2772–2778.
- Andrejczuk, M., W. W. Grabowski, S. P. Malinowski, and P. K. Smolarkiewicz, 2006: Numerical simulation of cloud–clear air interfacial mixing: Effects on cloud microphysics. *J. Atmos. Sci.*, **63**, 3204–3225.
- Ayala, O., B. Rosa, and L. Wang, 2008: Effects of turbulence on the geometric collision rate of sedimenting droplets. Part 2. Theory and parameterization. *New J. Phys.*, **10**, 075016, doi:10.1088/1367-2630/10/7/075016.
- Baker, M. B., and J. Latham, 1979: The evolution of droplet spectra and the rate of production of embryonic raindrops in small cumulus clouds. *J. Atmos. Sci.*, **36**, 1612–1615.
- , R. Corbin, and J. Latham, 1980: The influence of entrainment on the evolution of cloud droplet spectra. I. A model of inhomogeneous mixing. *Quart. J. Roy. Meteor. Soc.*, **106**, 581–598.
- Beard, K. V., 1976: Terminal velocity and shape of cloud and precipitation drops aloft. *J. Atmos. Sci.*, **33**, 851–864.
- , and H. Ochs, 1993: Warm-rain initiation: An overview of microphysical mechanisms. *J. Appl. Meteor.*, **32**, 608–625.
- Blyth, A., S. Lasher-Trapp, W. Cooper, C. Knight, and J. Latham, 2003: The role of giant and ultra-giant nuclei in the formation of early radar echoes in warm cumulus clouds. *J. Atmos. Sci.*, **60**, 2557–2572.
- Carpenter, R., K. K. Droegemeier, and A. M. Blyth, 1998: Entrainment and detrainment in numerically simulated cumulus congestus clouds. Part I: General results. *J. Atmos. Sci.*, **55**, 3417–3432.
- Caylor, I., and A. Illingworth, 1987: Radar observations and modelling of warm rain initiation. *Quart. J. Roy. Meteor. Soc.*, **113**, 1171–1191.
- Cooper, W., 1989: Effects of variable droplet growth histories on droplet size distributions. Part I: Theory. *J. Atmos. Sci.*, **46**, 1301–1311.
- , R. Bruintjes, and G. Mather, 1997: Calculations pertaining to hygroscopic seeding with flares. *J. Appl. Meteor.*, **36**, 1449–1469.
- Fankhauser, J. C., 1988: Estimates of thunderstorm precipitation efficiency from field measurements in CCOPE. *Mon. Wea. Rev.*, **116**, 663–684.
- Feingold, G., and P. Chuang, 2002: Analysis of the influence of film-forming compounds on droplet growth: Implications for cloud microphysical processes and climate. *J. Atmos. Sci.*, **59**, 2006–2018.
- Ferrier, B., J. Simpson, and W. Tao, 1996: Factors responsible for precipitation efficiencies in midlatitude and tropical squall simulations. *Mon. Wea. Rev.*, **124**, 2100–2125.
- Göke, S., H. Ochs, and R. Rauber, 2007: Radar analysis of precipitation initiation in maritime versus continental clouds near the Florida coast: Inferences concerning the role of CCN and giant nuclei. *J. Atmos. Sci.*, **64**, 3695–3707.
- Grabowski, W., O. Thouron, J.-P. Pinty, and J.-L. Brenguier, 2010: A hybrid bulk–bin approach to model warm-rain processes. *J. Atmos. Sci.*, **67**, 385–399.
- Illingworth, A. J., 1988: The formation of rain in convective clouds. *Nature*, **336**, 754–756.
- Jensen, J. B., and S. Lee, 2008: Giant sea-salt aerosols and warm rain formation in marine stratocumulus. *J. Atmos. Sci.*, **65**, 3678–3694.
- , P. H. Austin, M. B. Baker, and A. M. Blyth, 1985: Turbulent mixing, spectral evolution, and dynamics in a warm cumulus cloud. *J. Atmos. Sci.*, **42**, 173–192.
- Johnson, D. B., 1982: The role of giant and ultragiant aerosol particles in warm rain initiation. *J. Atmos. Sci.*, **39**, 448–460.
- Jonas, P., and B. Mason, 1982: Entrainment and the droplet spectrum in cumulus clouds. *Quart. J. Roy. Meteor. Soc.*, **108**, 857–869.
- , and —, 1983: Entrainment and the droplet spectrum in cumulus clouds—Reply. *Quart. J. Roy. Meteor. Soc.*, **109**, 899–900.
- Knight, C. A., J. Vivekanandan, and S. Lasher-Trapp, 2002: First radar echoes and the early Z_{DR} history of Florida cumulus. *J. Atmos. Sci.*, **59**, 1454–1472.
- Laird, N., H. Ochs, R. Rauber, and L. Miller, 2000: Initial precipitation formation in warm Florida cumulus. *J. Atmos. Sci.*, **57**, 3740–3751.
- Lasher-Trapp, S., C. Knight, and J. Straka, 2001: The formation of early radar echoes from ultragiant aerosol: Modeling and observations. *J. Atmos. Sci.*, **58**, 3545–3562.
- , W. Cooper, and A. Blyth, 2002: Measurements of ultragiant aerosol particles in the atmosphere from the small cumulus microphysics study. *J. Atmos. Oceanic Technol.*, **19**, 402–408.

- , —, and —, 2005: Broadening of droplet size distributions from entrainment and mixing in a cumulus cloud. *Quart. J. Roy. Meteor. Soc.*, **131**, 195–220.
- Lehmann, K., H. Siebert, and R. A. Shaw, 2009: Homogeneous and inhomogeneous mixing in cumulus clouds: Dependence on local turbulence structure. *J. Atmos. Sci.*, **66**, 3641–3659.
- Ochs, H., 1978: Moment-conserving techniques for warm cloud microphysical computations. Part II: Model testing and results. *J. Atmos. Sci.*, **35**, 1959–1973.
- Pinsky, M., A. Khain, and Z. Levin, 1999a: The role of the inertia of cloud drops in the evolution of the spectra during drop growth by diffusion. *Quart. J. Roy. Meteor. Soc.*, **125**, 553–581.
- , —, and M. Shapiro, 1999b: Collisions of small drops in a turbulent flow. Part I: Collision efficiency. Problem formulation and preliminary results. *J. Atmos. Sci.*, **56**, 2585–2600.
- Pruppacher, H., and J. Klett, 1997: *Microphysics of Clouds and Precipitation*. Springer, 954 pp.
- Saffman, P., and J. Turner, 1956: On the collision of drops in turbulent clouds. *J. Fluid Mech.*, **1**, 16–30.
- Shaw, R., 1998: Preferential concentration of cloud droplets by turbulence: Effects on the early evolution of cumulus cloud droplet spectra. *J. Atmos. Sci.*, **55**, 1965–1976.
- Small, J. D., and P. Y. Chuang, 2008: New observations of precipitation initiation in warm cumulus clouds. *J. Atmos. Sci.*, **65**, 2972–2982.
- Srivastava, R., 1989: Growth of cloud drops by condensation: A criticism of currently accepted theory and a new approach. *J. Atmos. Sci.*, **46**, 869–887.
- Straka, J., and J. Anderson, 1993: Numerical simulations of microburst-producing storms: Some results from storms observed during COHMEX. *J. Atmos. Sci.*, **50**, 1329–1348.
- Telford, J., and S. Chai, 1980: A new aspect of condensation theory. *Pure Appl. Geophys.*, **118**, 720–742.
- Twomey, S., 1966: Computations of rain formation by coalescence. *J. Atmos. Sci.*, **23**, 405–411.
- vanZanten, M. C., and Coauthors, 2011: Controls on precipitation and cloudiness in simulations of trade-wind cumulus as observed during RICO. *J. Adv. Model. Earth Syst.*, **3**, M06001, doi:10.1029/2011MS000056.
- Wang, L., O. Ayala, B. Rosa, and W. Grabowski, 2008: Turbulent collision efficiency of heavy particles relevant to cloud droplets. *New J. Phys.*, **10**, 075013, doi:10.1088/1367-2630/10/7/075013.
- Warner, J., 1969: The microstructure of cumulus cloud. Part I: General features of the droplet spectrum. *J. Atmos. Sci.*, **26**, 1049–1059.
- Woodcock, A., 1952: Atmospheric salt particles and raindrops. *J. Meteor.*, **9**, 200–212.
- , 1953: Salt nuclei in marine air as a function of altitude and wind force. *J. Meteor.*, **10**, 362–371.
- , 1978: Marine fog droplets and salt. *J. Atmos. Sci.*, **35**, 657–664.
- , R. Duce, and J. Moyers, 1971: Salt particles and raindrops in Hawaii. *J. Atmos. Sci.*, **28**, 1252–1257.